



Screening for high-performance piezoelectrics using high-throughput density functional theory

Rickard Armiento,¹ Boris Kozinsky,² Marco Fornari,³ and Gerbrand Ceder¹

¹*Department of Materials Science and Engineering, Massachusetts Institute of Technology, Cambridge, Massachusetts 02139, USA*

²*Research and Technology Center, Robert Bosch LLC, Cambridge, Massachusetts 02142, USA*

³*Department of Physics, Central Michigan University, Mount Pleasant, Michigan 48859, USA*

(Received 20 March 2011; revised manuscript received 1 June 2011; published 19 July 2011)

We present a large-scale density functional theory (DFT) investigation of the ABO_3 chemical space in the perovskite crystal structure, with the aim of identifying those that are relevant for forming piezoelectric materials. Screening criteria on the DFT results are used to select 49 compositions, which can be seen as the fundamental building blocks from which to create alloys with potentially good piezoelectric performance. This screening finds all the alloy end points used in three well-known high-performance piezoelectrics. The energy differences between different structural distortions, deformation, coupling between the displacement of the A and B sites, spontaneous polarization, Born effective charges, and stability is analyzed in each composition. We discuss the features that cause the high piezoelectric performance of the well-known piezoelectric lead zirconate titanate (PZT), and investigate to what extent these features occur in other compositions. We demonstrate how our results can be useful in the design of isovalent alloys with high piezoelectric performance.

DOI: [10.1103/PhysRevB.84.014103](https://doi.org/10.1103/PhysRevB.84.014103)

PACS number(s): 77.84.-s, 71.15.Nc

I. INTRODUCTION

Materials with high piezoelectric coefficients have a large technological interest and are used in many applications.¹⁻⁴ Since the discovery of the anomalously large piezoelectric effect in lead zirconate titanate (PZT) based compounds,⁵⁻⁷ a search has been ongoing to find other compounds with similar properties.⁸⁻¹⁸ One driving force for this effort has been the replacement of lead-based compounds for less toxic alternatives. A further motivation is the possibility to discover compositions with a similarly high piezoelectric response but having different material properties, e.g., the ability to operate in a different temperature range. Finding new such compositions would not only be of technological benefit but would also add to our understanding of the underlying mechanisms for piezoelectricity, and aid the development of future design strategies.

We undertake a search for new compositions in this paper by using the power of high-throughput density functional theory^{19,20} calculations. The last decades have seen a rapid increase of computational power and development of theoretical methods useful for predicting material properties through computation. This has allowed computational prediction of material properties to be scaled to rapidly screen hundreds or thousands of materials. The high-throughput approach has proven successful in other fields (see, e.g., Refs. 21-26), and the present work applies these methods to the field of high-performance piezoelectrics.

The basic mechanism behind the good piezoelectric performance in PZT-based compounds has been extensively explored.^{4,27-32} PZT is a solid solution of $PbZrO_3$ (PZ) and $PbTiO_3$ (PT). PT is ferroelectric in a tetragonally distorted perovskite structure, but when alloyed with PZ it becomes rhombohedrally distorted. The two phases are separated, at nearly equal concentrations of PT and PZ, by a morphotropic phase boundary (MPB).^{4,27-29} The phase boundary is (i) occurring quasicontinuously via an intermediate monoclinic phase, (ii) taking place over a very narrow concentration range,

and (iii) almost temperature independent. All these features are crucial for making PZT as industrially useful as it is. Under change in stress, a composition at, or near, the MPB moves over the narrow phase boundary, either toward the rhombohedral or tetragonal deformation. This phase transition alters the direction of the macroscopic polarization vector, which thus greatly changes its directional magnitude.³⁰⁻³² This enhanced electromechanical coupling at the MPB is exploited in, e.g., transducers and actuators.³

There is much experimental and computational work aimed at finding materials with PZT-like behavior.⁸⁻¹⁸ The focus has primarily been on materials with the perovskite crystal structure, shown in Fig. 1, since this structure can accommodate the crucial phase-change driven polarization rotation. To the authors' knowledge, despite major efforts, there exists to date no lead-free technological replacement for PZT. Two notable recent materials are the work by Saito *et al.*³⁴ on $(K,Na,Li)(Nb,Ta)O_3$ and the work of Liu and Ren³⁵ on $Ba(Ti_{0.8}Zr_{0.2})O_3-(Ba_{0.7}Ca_{0.3})TiO_3$. The former material is expensive and difficult to synthesize due to problems with vaporization of potassium oxide during sintering,^{36,37} and the latter has a MPB that is very temperature dependent. Both of these materials utilize relatively complicated isovalent alloys of several different perovskite materials. The difficulty to find materials with an MPB similar to the one found in PZT suggests that the lead-based compounds have properties that are quite unique in this context. By doing a systematic investigation of a large sample of compositions we can learn which combination of properties are specific to PZT, PZ, and PT, and thus are limiting factors in finding new MPB-based piezoelectric materials. While previous work has studied selected sets of compounds, the authors are not aware of any density functional theory survey of this magnitude with the aim of classifying ferroelectric perovskites for use in high-performance piezoelectrics.

This paper is structured as follows. In Sec. II we present our high-throughput framework and the primary screening criteria.

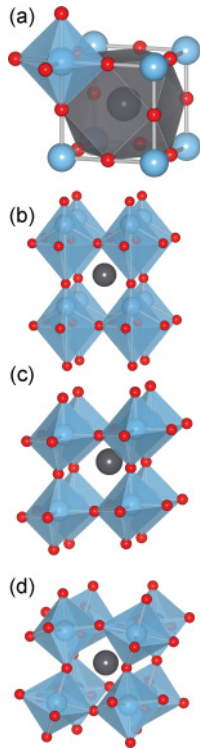


FIG. 1. (Color online) (a) The prototypical ideal perovskite structure ABO_3 . The figure shows the 12-coordinated A -site cation (big, black) and the 6-coordinated B -site cations (big, pale shaded/blue) which are embedded in octahedra (blue) defined by oxygens (small, dark/red). (b) The tetragonally distorted phase. (c) The rhombohedrally distorted phase. (d) The structure where the oxygen octahedra have been rotated along the $(1,1,1)$ direction. Note: the distortions are exaggerated for illustrative purposes as typical values of the rhombohedral tilt and tetragonal strain would not be visible. The figures were created using VESTA (Ref. 33).

In Sec. III we present the results of the computational survey. In Sec. V we discuss the results, first with focus on the properties that make PT and PZ special, and then we relate our results to the properties of isovalent alloys. Section V summarizes our main conclusions.

II. HIGH-THROUGHPUT METHODOLOGY AND SCREENING CRITERIA

Density functional theory (DFT)^{19,20} has been highly successful in describing ferro- and piezoelectric perovskite compounds.^{32,38–45} We have developed a high-throughput framework that automatizes the preparation of large batches of calculations for compositions on perovskite form. The calculations are executed on a Beowulf-type cluster. DFT calculations are performed with the Vienna *ab initio* simulation package, VASP 5.2.2,^{46–48} using the parameters described in the Appendix. The output is parsed by scripts that insert relevant data into a database. Database queries can then be used to analyze the results, screen for compositions with relevant features, and generate figures.

The high-throughput framework is used to consider every possible composition in the cubic ABO_3 perovskite form,

where A and B are any element up to bismuth (atomic number 83), except for hydrogen, helium, neon, argon, and krypton, and the lanthanides (lanthanum–lutetium). Compositions with lanthanides are excluded because the highly localized $4f$ electrons are difficult to treat with established DFT methods, and thus such compositions typically need a level of attention that is unavailable in high-throughput approaches. At this point we do not exclude any compositions which might require uncommon valence states to charge balance the compound. Hence, the complete chemical space is $63^2 = 3969$ compositions. Calculations of the energy of the cubic perovskites and the different distortions as well as the density of states are used to screen this set on the magnitude of the band gap and the energy differences between the distorted phases. This screening reduces the set to a manageable collection of 49 compositions. The details and motivations behind these two screening criteria and the calculations performed will be discussed below. Systems in the chemical space where the A - or B -site cation is in a highly unusual valence state are screened out by the requirement for a nonzero band gap.

Our first screening criterion is to require the perovskite compositions to be nonmetallic and have a band gap that is large enough to avoid current leakage when a potential is applied to the material, since that would preclude good piezoelectric performance. While the Kohn-Sham gap Δ_{KS} is a poor approximation of the fundamental band gap, the two quantities are correlated enough to motivate disregarding compositions with a particularly small Kohn-Sham gap. We have chosen the requirement that the Kohn-Sham band gap $\Delta_{KS} > 0.25$ eV, as this will avoid small gap semiconductors with significant conductivity coming from thermally excited carriers. For comparison, PZT has a fundamental gap of about 3 eV.⁴⁹ As will be further discussed in the next section, this requirement screens out a vast majority of the considered compositions, and will leave only 99 compositions to be further investigated.

The calculations of the Kohn-Sham band gap are performed using 5-atom primitive perovskite cells that are volume optimized under $Pm\bar{3}m$ symmetry (i.e., the prototypical cubic perovskite structure). We also perform calculations for two fixed distorted cells, one with a fixed tetragonal and another with a fixed rhombohedral distortion. The structures are taken as the ground state optimized structure of $BaTiO_3$ and $PbTiO_3$, respectively, scaled to the equilibrium volume found in $Pm\bar{3}m$ symmetry. These calculations are intended for finding cases when the ideal cubic perovskite structure has a small Kohn-Sham gap, but the lower symmetry configurations have a much larger one. The volume-optimized ground state energy in $Pm\bar{3}m$ symmetry is denoted E_0^{cub} .

Our second screening criterion is based on the work by Ghita *et al.*⁴⁵ They used DFT calculations to study the interplay between the A - and B -site displacements in the perovskite structure. They specifically stressed that the MPB could be identified from the energy differences between different distortions of the ideal perovskite structure. Of primary interest are tetragonal, rhombohedral, and rotational distortions, illustrated in Fig. 1. As discussed in the introduction, a compound that imitates the MPB of PZT needs to structurally transform between the different phases. To

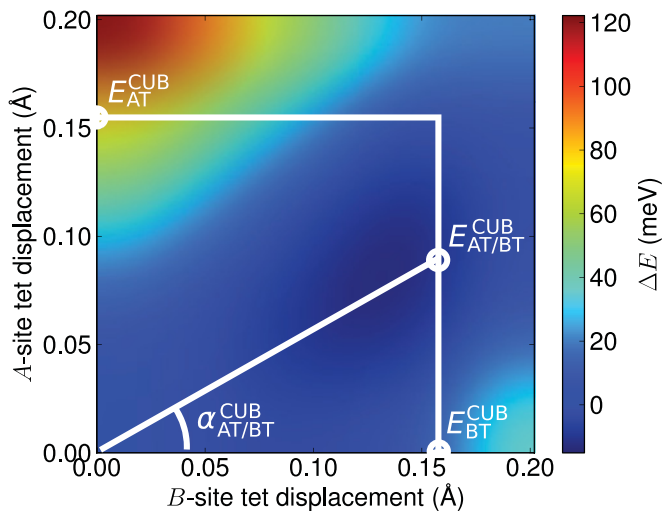


FIG. 2. (Color online) Key quantities in the energy landscape when the A - and B -site ions are displaced along the tetragonal $(1,0,0)$ direction in the cubic BaTiO_3 . For definitions of the quantities, see Sec. II.

optimize the piezoelectric performance, the energy difference between these phases should be as small as possible. If one of the phases is much lower than the others the structure will be too resilient to the structural changes needed for the transition over the MPB. We take as the relevant energy scale for phase energy differences 10–100 meV. Although the tetragonal and rhombohedral phases are of primary interest, the transition to rotationally distorted structures also needs to be available within the same energy scale, ~ 10 –100 meV, as it has been suggested that the rotation of oxygen octahedra is an important part of the transition between the rhombohedral and tetragonal phases over the MPB.^{50–53} The total span of the energies for the rhombohedrally, tetragonally, and rotationally distorted structures (i.e., maximum – minimum) is denoted as ΔE^P . We will use an inclusive cutoff that requires $\Delta E^P < 0.5$ eV, which, as will be discussed in the next section, brings down the number of interesting compositions from 99 to 49. We have not taken into account the possibility of significant additional energy barriers between the phases that are larger than the energy difference between the phases. However, prior work on the energy dependence of the rotation of the polarization vector indicates that there are no such significant barriers, cf. Ref. 31 (see, e.g., their Fig. 2).

To calculate the energies of the tetragonally and rhombohedrally distorted structures we start from fixed structures slightly distorted according to the desired symmetry, and then use ionic and cell-shape relaxation to find the minimum energy structure. The minimum energies in these distorted phases are denoted E_0^{tet} and E_0^{rho} , respectively. See the Appendix for more discussion on the details of the phase energy calculations. We also consider a structure where the oxygen octahedra are rotated along the $(1,1,1)$ direction. These calculations need 10-atom cells, and the ground state energy per ABO_3 formula unit in this distortion is denoted E_0^{rot} . Rotations along other vectors were considered for a few composi-

tions, but were always higher in energy. Using this notation we have

$$\Delta E^P = \max(E_0^{\text{rho}}, E_0^{\text{tet}}, E_0^{\text{rot}}) - \min(E_0^{\text{rho}}, E_0^{\text{tet}}, E_0^{\text{rot}}). \quad (1)$$

The calculations of distorted structures also directly give the minimum energy cell deformation parameters. We denote the rhombohedral deformation angle as α_{rho} , the angular rotation of the oxygen octahedra in the rotated structure as α_{111} , the ratio of the respective lattice constants in the tetragonal phase as c/a , and the displacement of the B -site ion with respect to the center of the oxygen octahedra in the tetragonal phase as Δd .

Ghita *et al.* also stressed the importance of the energy landscape as single ions are displaced in the cubic structure. They moved either the A - or the B -site ion in the ideal cubic ABO_3 perovskite structure along either the rhombohedral $(1,1,1)$ or the tetragonal $(0,0,1)$ axis in the conventional cell. In our framework we calculate these energy landscapes using an extended methodology where both the A - and B -site ions are displaced simultaneously. In this way the possible interaction between the two ions is also considered. Hence, the result is a two-dimensional energy landscape, where the x and y axes respectively correspond to the displacement of the B and A sites. From these calculations we extract a number of key quantities as illustrated in Fig. 2: $E_{\text{AT}}^{\text{cub}}$ is the energy when the A -site ion has been translated $0.3a$ in the tetragonal deformation direction $(0,0,1)$, and equivalently for the B site, $E_{\text{BT}}^{\text{cub}}$. (The designation “cub” is used to clarify that these calculations are done by displacing the ions within the ideal cubic cell shape.) Similar quantities, $E_{\text{AR}}^{\text{cub}}$ and $E_{\text{BR}}^{\text{cub}}$, can be defined when the translations are along the rhombohedral deformation direction $(1,1,1)$. Furthermore, we let $E_{\text{AT/BT}}^{\text{cub}}$ be the minimum energy when either the A - or the B -site ion is displaced $0.3a$ and the other is displaced somewhere in the range $(0-0.3)a$. An angle $\alpha_{\text{AT/BT}}^{\text{cub}}$ can now be defined in the energy landscape as the angle between (i) the line from the ideal structure with no displacement and the location of this minimum and (ii) the x axis which represents only B -site displacement. The angle describes the ratio of displacement between the A and B sites if the ions were to displace toward the energy minimum. To clarify, when the ions move to minimize the energy, if only the B site displaces, we get $\alpha_{\text{AT/BT}}^{\text{cub}} = 0^\circ$, if only the A site displaces, $\alpha_{\text{AT/BT}}^{\text{cub}} = 90^\circ$, and if they move equally, $\alpha_{\text{AT/BT}}^{\text{cub}} = 45^\circ$. Similar angles and energies can be defined in the energy landscapes along the other displacement directions, i.e., $E_{\text{AT/BR}}^{\text{cub}}$, $E_{\text{AR/BT}}^{\text{cub}}$, and $E_{\text{AR/BR}}^{\text{cub}}$; $\alpha_{\text{AT/BR}}^{\text{cub}}$, $\alpha_{\text{AR/BT}}^{\text{cub}}$, and $\alpha_{\text{AR/BR}}^{\text{cub}}$. Figure 2 shows the AT/BT quantities in an example energy landscape.

As a comparison, Fig. 3 shows the landscapes for PZ and PT. We stress that these calculations are not meant to create an accurate representation of the actual energy landscape as the structure is distorted. Rather, similar to the study of ionic displacement in the work of Ghita *et al.*,⁴⁵ the energy landscapes sample the energy response to the off-centering displacement of the cations. The cell is kept as an ideal cubic to isolate this energy response without influence from changes in the Bravais lattice. Hence, the energy landscape describes the interaction between the cations, electrostatically and through orbital hybridization with the oxygen. When the

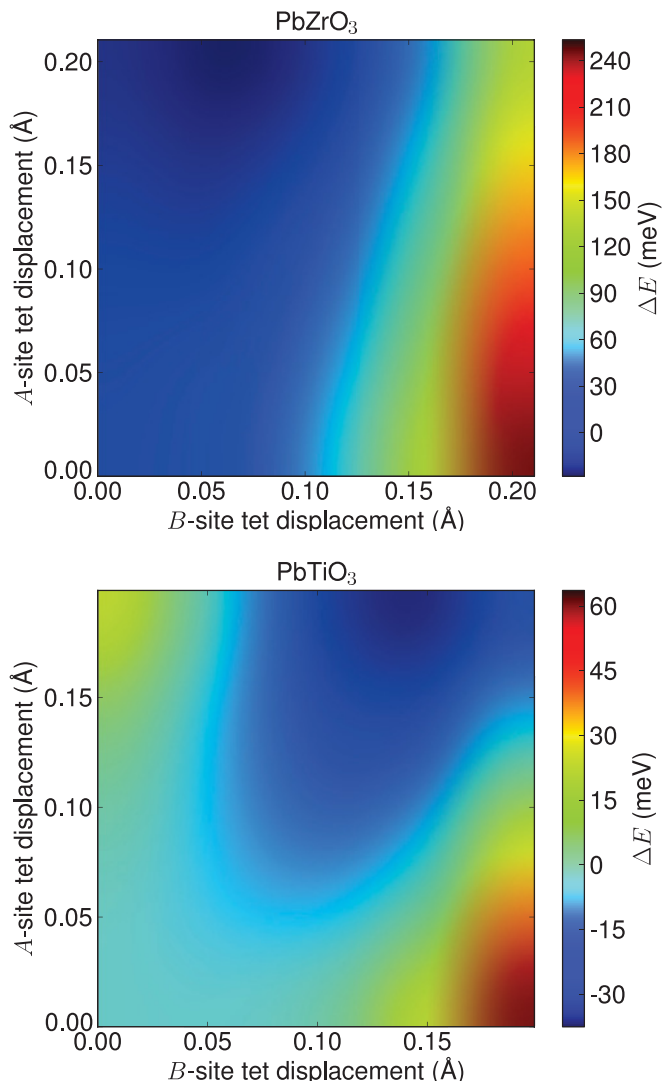


FIG. 3. (Color online) Energy landscapes when the A - and B -site ions in cubic PbZrO_3 and PbTiO_3 are displaced various distances along the tetragonal $(1,0,0)$ direction. For PbTiO_3 when both of the ions are displaced simultaneously (the energy values in the center of the 2D plot), the energy is lower than when they are displaced individually (the energy values along the x and y axes). This means that the interaction between the ions (electrostatic and bond interaction across the oxygens) makes it energetically favorable for both ions to move together. Using the key quantities defined in Sec. II and Fig. 2, this is indicated by $\alpha_{\text{AT/BT}}^{\text{cub}} \approx 45^\circ$, rather than 0° or 90° .

resulting energy landscape is flat, both cations are active in the polar distortion, and a significant displacement of the ions is possible and may make the tetragonal distortion favorable. When we consider materials relevant for forming an MPB, the overall energy scale and to what extent energy is gained when the A - and B -site ions are displaced together are of primary importance. This will be further discussed in connection to our results in Sec. IV.

It has not been a primary goal of the present high-throughput screening to carefully consider stability as a criterion. The reason is that these compounds will be discussed as possible components of alloys, which may be stable even if the

isolated components are unstable. As an example, consider the tetragonal alloy used in the material by Saito *et al.*³⁴ It consists of $\text{KNbO}_3 + \text{LiNbO}_3$, which forms a tetragonal material because the compounds have the right energy features; i.e., LiNbO_3 strongly prefers a tetragonal structure and the energy landscape is very PT-like.⁵⁴ However LiNbO_3 is not stable in perovskite form. Hence, to be able to use our results as possible components of alloys, we cannot exclude compositions based on their stability. Rather, a stability requirement needs to be applied to the final alloy.

Further quantities calculated for our selected set of compositions include the spontaneous polarization and Born effective charges. These calculations are implemented in the VASP electronic structure software. For more details on these calculations, see the Appendix.

The presented calculations use the DFT functional by Perdew, Burke, and Ernzerhof (PBE).⁵⁵ PBE is extensively used in the field and has a proven reliable track record for these applications when the volume is restricted during relaxation as described in the Appendix. However, more recent functionals that require the same computational effort as PBE have shown improved performance for solid state calculations, e.g., the Armiento-Mattsson functional (AM05) from 2005,^{56,57} the Wu-Cohen functional (WC) from 2006,⁷⁶ and a revised version of PBE by Perdew *et al.* from 2008 (PBEsol).⁵⁸ The WC functional has been shown to perform well for volume, strain, and other relevant properties for PbTiO_3 and BaTiO_3 .^{59,76} However, none of these functionals have been as thoroughly applied to perovskite systems as PBE, and a high-throughput study such as the present one would be less useful if it were based on methods not already established as uniformly reliable.

III. RESULTS

Removing perovskites for which the Kohn-Sham band gap $\Delta_{\text{KS}} < 0.25$ eV leaves only 99 out of the 3969 possible ABO_3 compositions. While this is a straightforward requirement, one may raise the concern that for a specific structure, some of the considered distortions of the perovskite structures may give a large band gap, while others do not. As was discussed in the previous section, to study this issue, we have also calculated each composition using a fixed rhombohedrally and a tetragonally distorted structure (using, respectively, the ground state optimized structure of BaTiO_3 and PbTiO_3 , adjusted for volume). We found only two compositions which are metallic in the cubic phase but which have a Kohn-Sham gap $\Delta_{\text{KS}} > 0.25$ eV in both the tetragonal and rhombohedral phases. These are MgMnO_3 , CaMnO_3 . Both of these are magnetic manganese compounds and may be useful as, e.g., alloy end points for multiferroics. There are two other compositions that have a small gap in the cubic phase $\Delta_{\text{KS}} < 0.25$ eV but a larger gap in the distorted phases $\Delta_{\text{KS}} > 0.25$ eV; these are RbVO_3 and CdGeO_3 . In the present investigation these four compositions have been disregarded to avoid the difficulty of dealing with the metallic cubic phase. Due to their relatively small Kohn-Sham gaps (all < 0.6 eV), neither of these are expected to be very relevant for high-performance piezoelectrics, but they may be important for other applications. A different concern, although not expected,

is whether compositions that are nonmetallic in the cubic phase can turn metallic under distortions. No such cases are found in our data set.

For the remaining 99 compounds, the Kohn-Sham gap size and the lowest phase energy are illustrated in Fig. 4. In Fig. 4(a) all the combinations of *A*-site (the *y* axis) and *B*-site (the *x* axis) species on ABO_3 form that give nonmetallic compositions are represented. Most of the *B* sites found can be recognized as commonly occurring in the literature on perovskites, most prominently, e.g., the zirconates, titanates, niobates, and silicates. In general there is a large spread of Kohn-Sham gap values, even within compositions sharing *A* or *B* sites (i.e., within the same column or row in the figure). The largest gaps are found among the hafnates with Ca, Sr, Ba, or Li on the *A* site. In Fig. 4(b) the compositions are colored according to the distortion with the lowest energy. We see that only 11 compositions have the tetragonal distortion as its lowest energy, highlighting that finding a direct replacement of PT in PZT among the pure ternary perovskites is unlikely. Note that while the band gap calculations for selecting these compositions are performed using fixed distorted cells, the phase energies presented in Fig. 4(b) are fully relaxed with respect to cell-shape and ionic positions constraining the symmetry appropriately.

As discussed in the previous section, the next screening criterion is based on the phase energy differences, motivated by the need for a small energy scale for crystal deformation. Again, a somewhat arbitrary but inclusive cutoff is used, $\Delta E^P < 0.5$ eV, which requires the difference between largest and smallest of the energies of the three distorted structures to be small (rotational, rhombohedral, and tetragonal). This screening leaves 49 compositions for further study.

Figure 5(a) shows ΔE^P for the 49 selected compositions, with the color reflecting the structure with the lowest energy. The value of ΔE^P for PT and PZ are among the smaller ones. It is relevant to look at the influence of cell volume on these results, since, if the cell volume is expanded, the increased freedom for the *B* site to move in the structure is expected to favor a polar off-centering displacement. Volume increase may thus lower the energy of the tetragonal phase. Correspondingly, a smaller volume is expected to promote rotational distortion.⁴⁵ These expectations are confirmed in our set of compositions when we calculate the phase energies for expanded (+10%) and compressed (−10%) cell volumes, which are shown in Figs. 5(b) and 5(c). These figures show the extremes of the effect on phase energies by volume change. While 10% volume change corresponds to unphysically large external pressures, volume changes on this order may still be relevant when considering alloys of materials that are mismatched in volume.

Out of the selected compositions none are predicted as magnetic by our calculations. In the larger set of 99 compositions in Fig. 4, only 10 are magnetic, the 6 with Mn, and the 4 with Tc on the *A* site.

For the 49 selected compositions we have calculated a number of relevant properties shown in Fig. 6. The figure encompasses five property categories. The first category, “Energetics,” shows the various phase energies. The energy for all distortions is referenced with respect to the cubic phase, which represents the maximum energy, as all distorted phases can relax to cubic structure when favorable (this happens, e.g.,

in the case of $BaZrO_3$). In this category one can for each composition see the difference in energy between the phase that has the highest energy and the phase that has the lowest energy. The difference between these two energies is the phase energy span ΔE^P .

The second category of Fig. 6, “Deformation,” shows key quantities of the distorted perovskite cell for the various phases. It has been suggested that the amount of deformation of the ideal perovskite structure is a major factor in ferroelectricity.³⁸

The third category of Fig. 6, “*A*-*B* interplay,” shows the key quantities extracted from the ionic displacement energy landscapes as illustrated in Fig. 2. The values shown are extracted from the energy landscape where both the *A* site and *B* site are moved in the tetragonal direction. Energy values shown in this category are from the fixed 5×5 grid used for the calculations. For the compositions with very flat energy landscapes, Fig. 7 gives a more detailed view that includes the key quantities for other displacement directions. The key quantities of the energy landscapes for the four different displacement directions shown in the four columns appear to be very similar. A closer examination shows that the AT/BT and AR/BT columns are almost indistinguishable, as are AR/BR and AT/BR. However, when the direction in which the *B* site is displaced ($AT/BT \rightarrow AT/BR$ and $AR/BR \rightarrow AR/BT$) the variation is larger, on the order of 5 meV. This observation will be further discussed in Sec. IV.

The fourth category of Fig. 6, “Polarization,” shows the Born effective charge for the *A* and *B* sites, Z_B^* , Z_A^* , and the spontaneous polarization in the tetragonal phase P_s . The nature of the *A* cation appears to have little influence on the value of Z_B^* . Compounds with Pb on the *A* site tend to have the larger Z_A^* .

The fifth category of Fig. 6, “Structure,” shows estimates for the stability of the compositions, their Kohn-Sham gap, and their volume. Here, $t_6 = (r_6^A + r_6^O)/[\sqrt{2}(r_6^B + r_6^O)]$ is the tolerance factor proposed by Goldschmidt⁶², where r_6^A , r_6^B and r_6^O are the ionic radii of *A*, *B*, and O, respectively. Similar to other work using the tolerance factor as a measure for stability of perovskites, we use the 6-coordinated Shannon ionic radii⁶³ for all the sites, despite the fact that the ideal cubic perovskite structure has the *A* site in a 12-coordinated configuration. The motivation for this is that most perovskites are in distorted phases, where the coordination on the *A* site is lower. We also present the stability criteria of Li *et al.*⁶¹ A circle for “Stability” marks that the values of the tolerance factor and of an “octahedral factor” r_6^B/r_6^O are within the limits derived in Ref. 61 for a composition to be predicted to exist as a stable perovskite. The volume V is the volume relaxed under $Pm3m$ symmetry, which is used for all the distorted structures. The Kohn-Sham gap Δ_{KS} is calculated in the ideal cubic perovskite configuration.

IV. DISCUSSION

In the following, we will first discuss our results with a focus on the properties of the individual compositions when compared to the well-known compounds relevant for high piezoelectric performance: PT and PZ. Subsequently, we

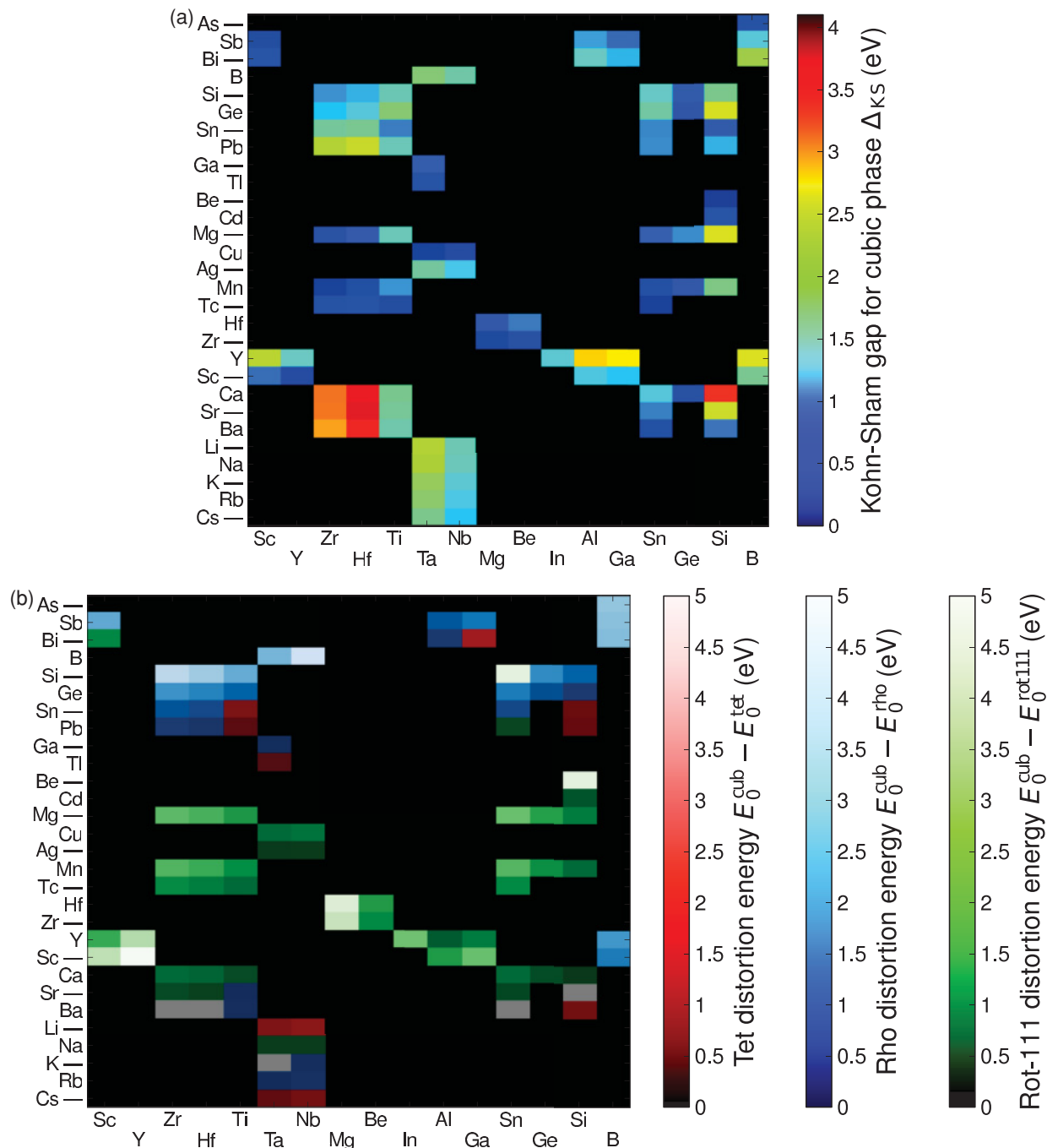


FIG. 4. (Color) The 99 ternary perovskite oxides out of the chemical space of 63^2 that are predicted as nonmetallic by our DFT calculations. The x axis is the A -site species, and the y axis is the B -site species, ordered by Mendeleev number which keeps chemically similar species together (Ref. 60). The color shows (a) the band gap for the cubic structure and (b) the energy of the lowest distorted phase. Compositions with no Kohn-Sham gap are shown as black. Rows and columns that would have been completely black are excluded from the plots. In (b) compositions that stay cubic when they are allowed to distort are marked as gray.

will discuss how our results help understand and predict the properties of the isoivalent alloys.

A. Properties of individual compositions

We first consider the 49 selected nonmetallic compositions shown in Fig. 5. The components of PZT, PT, and PZ show up as materials where the tetragonal and rhombohedral

distortions are lowest in energy. However, in its pure form PZ is antiferroelectric and has an orthorhombic distortion.^{64,65} In the present study we have restricted ourselves to a set of distorted phases relevant for observing the rhombohedral-tetragonal MPB transition, and of these phases the rhombohedral is lowest in energy for PZ.

In Fig. 6 we can see that out of the 49 compositions selected for their low phase energy differences, many have phase

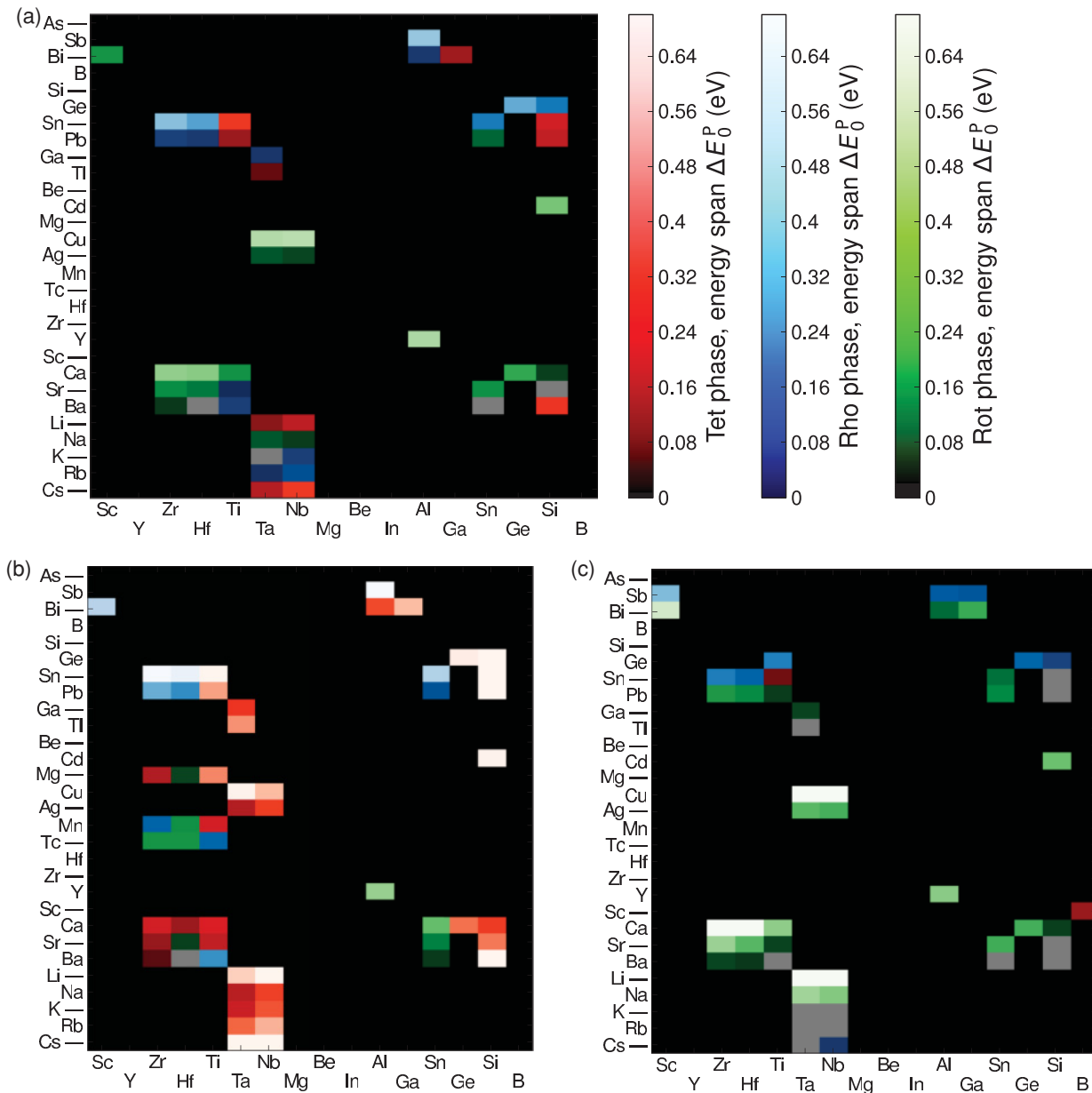


FIG. 5. (Color) (a) The span of phase energies (highest-lowest) ΔE^P for the 49 nonmetallic ternary perovskite oxides from Fig. 4(b) with $\Delta E^P < 0.5$ eV. The color indicates which of the phase energies is the lowest. (b) ΔE^P for structures at 10% expanded volume, using the same criteria. (c) ΔE^P for structures at 10% compressed volume, using the same criteria. Compositions that stay cubic when they are allowed to distort are marked as gray.

energies that are much larger than PZ and, in particular, PT. The PZ and PT structures have significant deformation, meaning that the energy dependence on deformation for these structures is low compared to other compositions. Hence, our results corroborate the picture that being able to transform between phases which are similar in energy is a crucial prerequisite for forming a MPB.

In most perovskites the main contribution to the polarization comes from the displacement of the B -site ion. In our data set the values of Z_B^* are very similar between compositions that share B -site species, and seem largely independent of the value of the Born effective charge for the A -site Z_A^* . This is not surprising when Z_B^* is close to the nominal charge of the

B -site ions. However, we find that this is true also when Z_B^* is anomalously high (i.e., much higher than the associated ionic state). Values of Z_B^* much higher than the associated ionic state are a prerequisite for high piezoelectric performance.^{30,31} The argument made is that the Born effective charge represents the charge being displaced as the B site moves in the structure, and the more charge is displaced, the greater is the resulting change in polarization. We see that both the titanates and the zirconates have this anomalously high Born effective charge, but, e.g., the aluminates and silicates do not. Hence, as a criterion, it appears that the Born effective charge can be used to promote certain B -site species over others, almost independently of the A -site species.

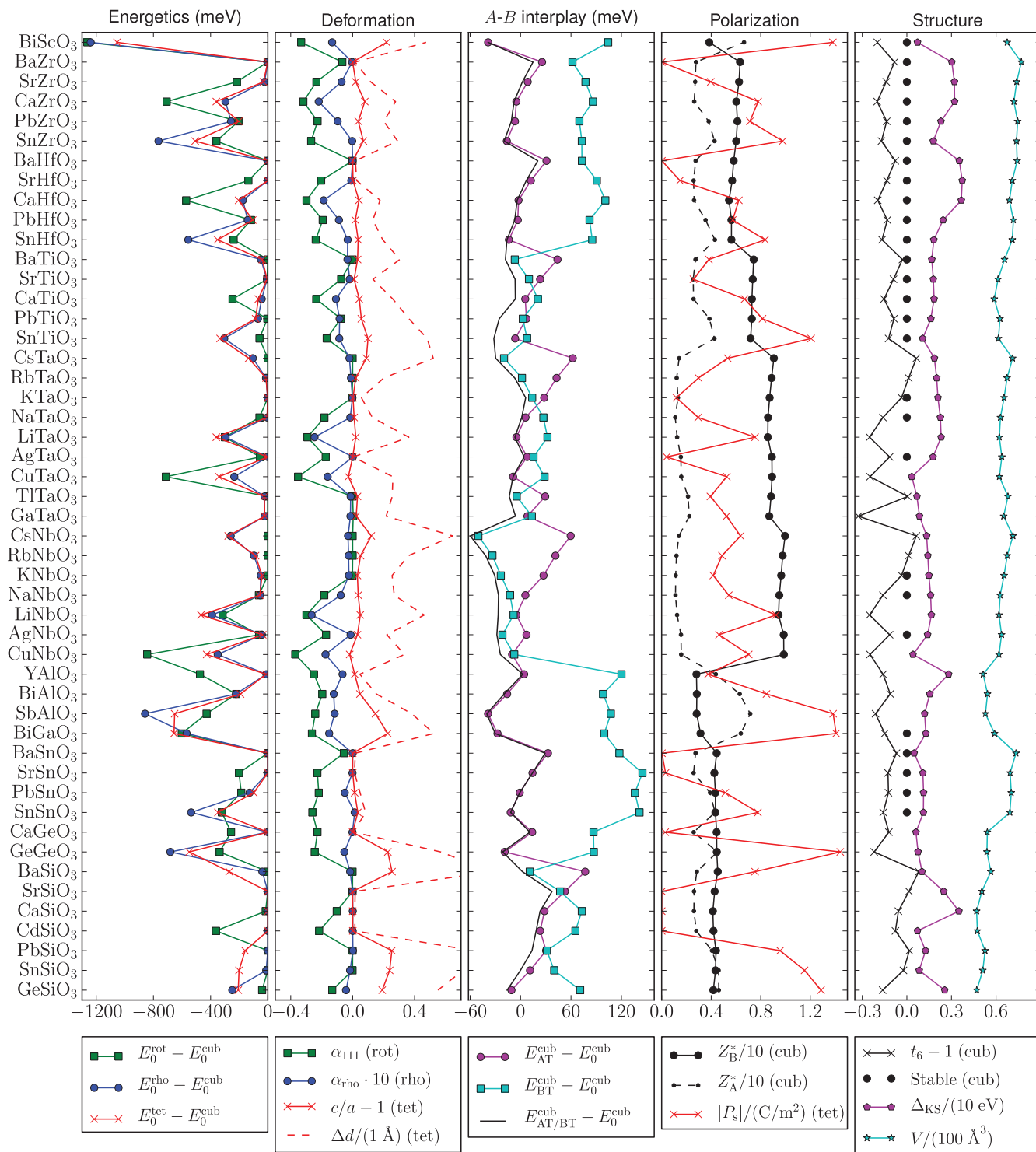


FIG. 6. (Color online) Calculated properties of the selected 49 nonmetallic ternary perovskite oxides. The compositions are listed in order of Mendeleev number (Ref. 60) on the B-site first, and on the A-site second. The quantities are divided into five categories defined and discussed in Sec. II. A “•” symbol for “Stable” indicates that the composition is a formable perovskite according to the criteria of Ref. 61. As indicated in the legends, some quantities have been rescaled to fit the scales used.

The polarization of perovskites has been discussed in terms of a pseudo-Jahn-Teller effect⁶⁶ where the cross-gap hybridization between oxygen 2*p* states and empty *d* states of the B-site ion promotes ferroelectricity.³⁸ For all our selected compositions there are common nominal valences that result

in an empty valence *d* shell on the B cation, with the possible single exception of GaTaO₃, where if Ga is in its most common 3+ state, the nominal state of Ta is a 5*d*² configuration. However, it is possible that Ga is in a more unusual 1+ state, making the 5*d* shell of Ta empty. Hence, our screening

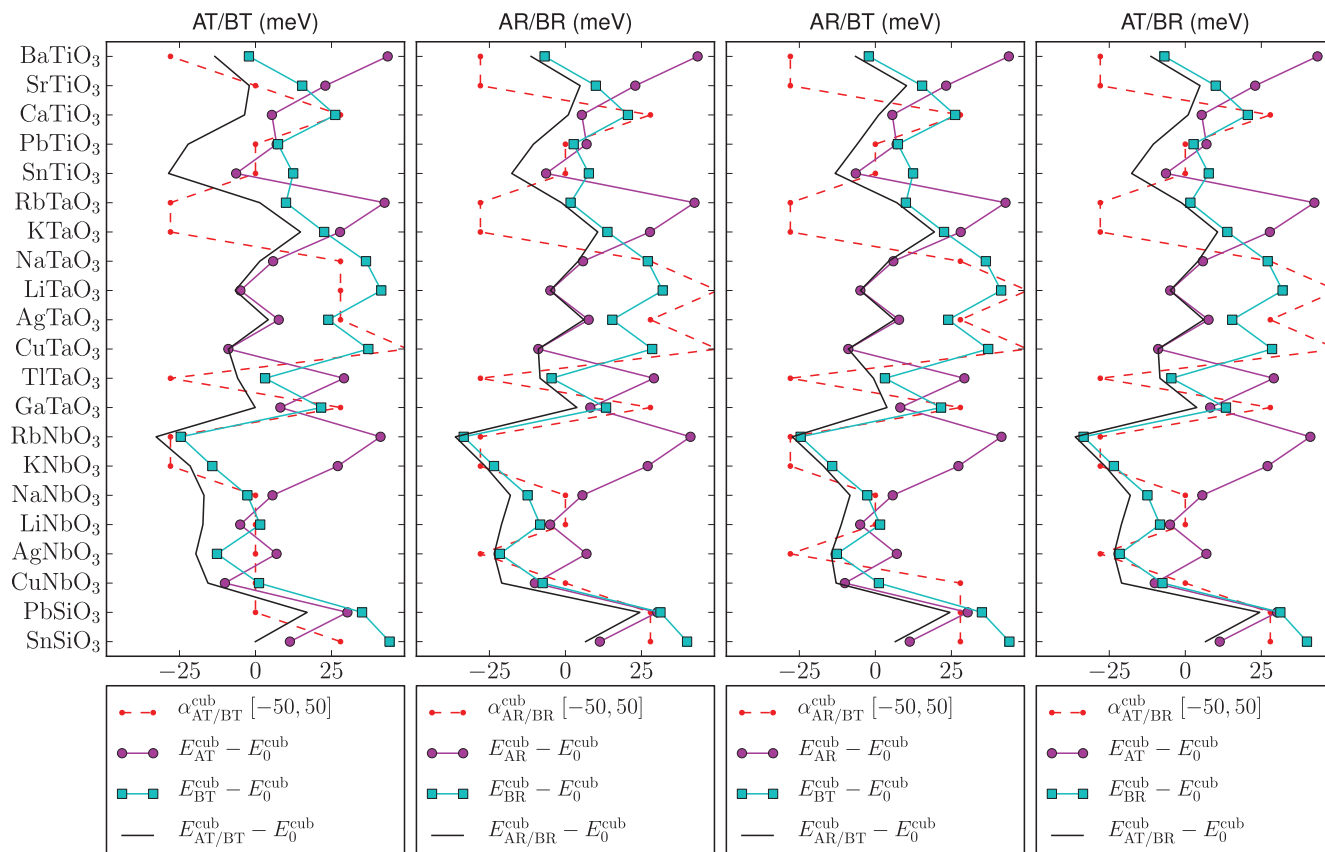


FIG. 7. (Color online) A closer look at the A - B site interplay for those compositions where the energy landscape is on a small scale, $E_{AT}^{\text{cub}}, E_{BT}^{\text{cub}} < 50$ meV. The plotted quantities are defined and discussed in Sec. II. The energy minimum used to calculate the angle $\alpha_{AT/BT}^{\text{cub}}$ is taken on the fixed grid used for the energy landscapes, which means that only 5 different values are possible for this angle, 0° , 27° , 45° , 63° , or 90° . For these values to fit on the scale in the figure, they have been scaled to the range -50 to 50 .

criterion appears to strongly favor compounds with empty d shells available for cross-gap hybridization.

In the ‘‘Polarization’’ column of Fig. 6, the spontaneous polarization in the tetragonal phase, P_s , is correlated with the displacement of the B -site species, indicating that B -site displacement is, as expected, the major source of polarization. However, there also appears to be some correlation with the value of Z_A^* , indicating that in most of the selected compositions the displacement of the A site is also important. The spontaneous polarizations of PT and PZ are among the larger of the selected compounds. This is expected, as a large spontaneous polarization should be important to maximize the electromechanical coupling. Furthermore, due to the importance of cross-gap hybridization discussed above, one may expect a relation between the size of the gap and the spontaneous polarization. By comparing columns 2 and 3 of Fig. 6 it is possible to find some support for an increased gap giving a lower spontaneous polarization.

For the A - B interplay, Ghita *et al.* argues that the polarization in perovskite compounds emerges from an energy landscape that makes it energetically favorable for ions to displace toward their location in the distorted structure;⁴⁵ i.e., for a compound that is tetragonal in its ground state, the energy should decrease when starting from the ideal cubic structure and displacing the A and B site ions along the tetragonal distortion direction $(0,0,1)$. In Fig. 5 this feature

of the energy landscape is identified by small negative values for $E_{AT/BT}^{\text{cub}} - E_0^{\text{cub}}$ in the Interplay column. In this figure we can also see whether it is energetically favorable for the ions to displace together. This case is identified by comparing the value of $E_{AT/BT}^{\text{cub}}$ (black line), which represents the landscape minimum energy, with the values for the individual A - and B -site displacements, i.e., E_{AT}^{cub} and E_{BT}^{cub} (cyan and purple lines). If the former is significantly lower than the latter, it is favorably for both ions to move together and find the minimum energy in the energy landscape. Looking at the more detailed Fig. 7, PT has among the strongest energy decrease when displacing both the A and B sites simultaneously.

In most compositions the relation between the ionic size of the A and B cations does not perfectly fit the one for the ideal perovskite structure, and thus the displacement of one of the sites will be more restricted than the other. The ion that is less space restricted typically leads the distortion, which gives the classification of compositions as A - or B -site active. Since the governing energy contribution to the energy landscape can be interpreted as representing the size restriction, these alternatives directly correspond to the angle $\alpha_{AT/BT} < 45^\circ$, $\alpha_{AT/BT} > 45^\circ$, or $\alpha_{AT/BT} \approx 45^\circ$. In Fig. 7 the angle is rescaled so 45° is represented by 0, and we find that PT is one of the few selected compositions classified as having a balanced ionic size.

Figure 6 shows that the energy landscape dependence on the B -site displacement E_{BT}^{cub} is mostly determined by the B -site species, which matches our observation for Z_B^* . Furthermore, we find that the larger E_{BT}^{cub} is, the smaller the value of Z_B^* is. For example, the smallest value of E_{BT}^{cub} is found for CsNbO_3 , and the group of niobates has the largest Z_B^* of all B cations. Progressing in order through B cations with smaller values of Z_B^* , i.e., the tantalates, titanates, hafnates, and zirconates, we successively find for each such group larger values of E_{BT}^{cub} . However, the trend is less clear for the aluminates and silicates, which all have a B -site species that does not have Z_B^* larger than the nominal ionic charge. As a possible explanation we speculate that the larger Z_B^* is relative to its nominal charge, the more covalent in nature the B -site-oxygen bond is. A covalent bond favors an off-centering displacement of the B site and thus gives the negative correlation between E_{BT}^{cub} and Z_B^* that we observe. If this connection between covalency and off-centering displacement is correct, other effects apparently enter for the almost completely ionic bonds in aluminates and silicates where Z_B^* is approximately equal to the nominal charge.

As we remarked in Sec. III, there is a strong similarity between the key quantities of the energy landscapes for the four different displacement directions shown in the four columns of Fig. 7. Closer examination shows that the AT/BT and AR/BT columns are almost indistinguishable, as are AR/BR and AT/BR. However, when comparing these two groups, we see a difference of about 5 meV in the energy quantities. This means that there is an overall anisotropy between the displacement along the A and B sites, but that anisotropy is weaker for the A site than for the B site. The difference in the anisotropy between displacing the A and B sites was also observed by Ghita *et al.*⁴⁵ for the compounds they investigated. Related observations of how the energy landscapes are isotropic for ionic displacement in layered perovskite structures were reported by Nakhmanson and Naumov, who connected the results to the Goldstone theorem.⁶⁷

The last column in Fig. 6, “Structure,” shows the tolerance factor and a stability criteria to help judge which compositions are possibly stable in their pure form. These stability measures are highly approximate, but, as was explained in Sec. II, a very careful assessment of stability is less useful when compositions are considered as possible alloy components.

B. Implications for isovalent alloys

One can understand the approach taken to create the two recently proposed MPB-based piezoelectric materials^{34,35} as composing two separate alloys for the two sides of a MPB, and then interpolate the concentration continuously between these two alloys to find a phase boundary. In this approach the alloys closely mimic the roles of PZ and PT in PZT. In Refs. 34,35 each of the materials on either side of the MPB have been created as an isovalent substitution of one perovskite composition into another (the exact compositions of these materials will be discussed in detail below.) Hence, our list of selected compounds can be interpreted as a list of relevant alloy components for such alloys. We will in the following discuss the implication of our results for this type of isovalent alloy. The use of heterovalent alloys for PZ- or

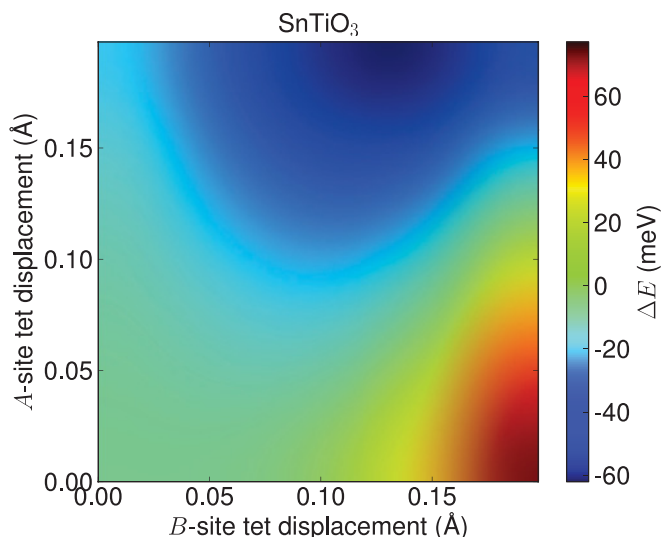


FIG. 8. (Color online) Energy landscape when the A - and B -site ions in cubic SnTiO_3 are displaced various distances along the tetragonal (1,0,0) direction. This energy landscape has a strong resemblance to that of PbTiO_3 , shown in Fig. 3.

PT-like materials is not considered here. Heterovalent alloys are more complex to handle, as their electronic properties cannot be predicted as a straightforward combination of the properties of the constituent ternary perovskites.

The most straightforward type of isovalent perovskite alloy can be created as a combination of two pure ternary perovskites where one of the ions, on either the A or B site, remains the same, while the other site is substituted for an alternative ion of the same charge. In our diagram over all the possible alloy components, Fig. 5, such substitutions are either found in the same row, which means that they share the A site, or in the same column, which means that they share the B site.

Looking at the regular, as well as the volume expanded and compressed, results shown in Fig. 5 gives us an indication of how relevant alloys can be constructed. For a PT-like material, a compound that is tetragonal at least in the volume-expanded diagram is needed (under the assumption that the other component expands the volume of the compound), and similarly for the rhombohedral case, one of the compounds needs to be rhombohedral at least in one of the figures. This straightforward analysis identifies three groups which appear most promising.

The first group is in the upper left of the diagram, $(\text{Sn,Pb})(\text{Zr,Hf,Ti})\text{O}_3$. This small group contains PZT. The similarity between PT and SnTiO_3 seen for most properties in Fig. 6 appears to motivate an attempt to substitute Sn for Pb in PT. The A - B interplay landscapes are also similar between PbTiO_3 and SnTiO_3 , which are shown in Fig. 3 and Fig. 8. However, this substitution has proven difficult in practice, since Sn tends to go to the B site in such alloys.⁶⁸ Our stability results hint at this, since SnTiO_3 is not predicted as stable, but many of the compositions with Sn on the B site are. Furthermore, Hf appears as a possible B -site substitution that potentially could find use in altering the properties of the MPB. The energetics and A - B interplay data in Fig. 6 point to it behaving similarly to Zr. This observation is consistent with experimental results on PbHfO_3 .⁶⁹

The second group is in the lower left of the diagram, $(\text{Ba}, \text{Sr}, \text{Ca})(\text{Zr}, \text{Hf}, \text{Ti})\text{O}_3$. This group contains the alloys proposed by Liu and Ren,³⁵ where $\text{Ba}(\text{Ti}, \text{Zr})\text{O}_3$ is rhombohedral and $(\text{Ca}, \text{Ba})\text{TiO}_3$ is used as a tetragonal material. At their regular volumes, none of the components in the $(\text{Ca}, \text{Ba})\text{TiO}_3$ alloy have the tetragonal phase as the one lowest in energy. However, the larger cell volume of BaTiO_3 expands the volume of CaTiO_3 , and as seen in the expanded volume diagram of Fig. 5(b), its tetragonal phase then becomes lowest in energy. BaTiO_3 on the other hand is compressed by the presence of CaTiO_3 , which makes its phase energy span ΔE^P even smaller, as seen in Fig. 5(c). The alloy $(\text{Ca}, \text{Ba})\text{TiO}_3$ thus becomes a tetragonal material in its ground state. Furthermore, it appears that Sr and Hf could work as substitutes in alloys like the one proposed by Liu and Ren, which possibly could help improve the composition dependence of the MPB they found.

The third and final group is $(\text{Li}, \text{Na}, \text{K}, \text{Rb}, \text{Cs})(\text{Ta}, \text{Nb})\text{O}_3$, where we find the components in the material by Saito *et al.* $(\text{K}, \text{Na}, \text{Li})(\text{Nb}, \text{Ta})\text{O}_3$.³⁴ Their work essentially explores this complete group, barring the use of Rb and Cs, which arguably may be of less industrial interest. We can understand their work as starting from KNbO_3 , which is a stable rhombohedral perovskite, and adding a small amount (a ratio of 3%–6% on the A site) of the unstable but tetragonal LiTiO_3 . The properties of this alloy can be explained from our data as a straightforward combination of the phase energy differences for the compositions (cf. Fig. 5). The strong preference for the tetragonal phase of LiTiO_3 dominates the small phase energy differences found for both KNbO_3 and NaNbO_3 , making the combination a tetragonal compound. For a deeper discussion on the energetics and distortions of the $\text{KNbO}_3 + \text{LiNbO}_3$ alloy, see Ref. 54.

While our work identifies all the alloy components of three of the compounds published by Saito *et al.*, named LF1, LF2, and LF3 in their paper, they present an LF4 compound which adds a small ratio (4%) of Sb on the B site, which is not found as a component in our list of selected compositions. We will shortly address why this component is not identified by our work. All the compounds presented in Ref. 34, LF1–LF4, derive their piezoelectric response from the MPB created from the polarization vector change in the solid solution between $(\text{K}, \text{Na})(\text{Nb}, \text{Ta})\text{O}_3$ and $\text{Li}(\text{Nb}, \text{Ta})\text{O}_3$. Hence, the precise role of the added Sb is not clear to us, but it further improves the piezoelectric performance of the compound. This type of optimization by impurities is common also for high-performance PZT, where, e.g., a small amount of La is introduced to further improve the piezoelectric performance over that of pure PZT. It has not been our goal in this work to identify all such possible impurities for optimizing the piezoelectric performance of a MPB, only to identify the compounds that lead to the MPB formation.

We can also see in Fig. 5 that niobates with Cu, Ag, Ga, or Tl on the A site, and tantalates with Cu, Ag, or Ga on the A site could be considered as possible dopants in compositions in the group $(\text{Li}, \text{Na}, \text{K}, \text{Rb}, \text{Cs})(\text{Ta}, \text{Nb})\text{O}_3$. The fact that these dopants appear to promote tetragonality under expansion in Fig. 5(b) makes them especially interesting. These suggested substitutions appear to be less explored in literature and may present some opportunity to find new alloys with MPBs.

However, the dopants are likely to only be useful in smaller concentrations, since most of them are predicted to be unstable by the measure used for “Stability” in Fig. 6.

Apart from the groups explored above, it appears hard to find a stable tetragonal material among the remaining compositions, where many have low energies for the rotational distortion even at expanded volumes. A possible exception is the compositions $(\text{Bi}, \text{Sb})(\text{Al}, \text{Ga})\text{O}_3$. However, Fig. 6 shows that Al and Ga lack the anomalously large B-site Born effective charge that is found for e.g., Ti, Nb, and Ta.

V. SUMMARY AND CONCLUSIONS

In this work we have used a large-scale high-throughput DFT framework to investigate the space of pure ternary perovskite oxides. We discussed and examined the need for compositions with PZT-like MPBs to be nonmetallic and to have distorted phases separated by small energy differences. These criteria were used to pick out a set of 49 compositions that can be seen as the fundamental building blocks of isovalent alloys for compounds forming MPBs suitable for high piezoelectric performance. Within this set we could successfully identify the components of the three currently well-known compounds that accommodate a MPB of the type found in PZT.

For the 49 selected compositions we computed properties related to the piezoelectric performance in five categories: energetics, deformation, A-B interplay, polarization, and structure. We discussed the relation between these properties and the formation of MPBs, and identified three primary composition groups for isovalent alloys of these compositions, $(\text{Sn}, \text{Pb})(\text{Zr}, \text{Hf}, \text{Ti})\text{O}_3$, $(\text{Ba}, \text{Sr}, \text{Ca})(\text{Zr}, \text{Hf}, \text{Ti})\text{O}_3$, $(\text{Li}, \text{Na}, \text{K}, \text{Rb}, \text{Cs})(\text{Ta}, \text{Nb})\text{O}_3$, which coincide with three known materials with MPBs. Hence, a methodology has been presented that is useful for identifying and predicting compound alloys that can form MPBs from large-scale high-throughput calculations.

ACKNOWLEDGMENTS

The authors are grateful for funding provided by Robert Bosch LLC. The authors thank Samed Halilov for fruitful discussions. R.A. also thanks Predrag Lazić for helpful comments.

APPENDIX COMPUTATIONAL DETAILS

We perform spin-polarized DFT calculations^{19,20,70,71} in the plane-wave pseudopotential formulation of DFT as implemented in the Vienna *ab initio* simulation package (VASP 5.2.2). We use the projector augmented wave pseudopotentials^{72,73} that are distributed with VASP. Our calculations use the functional by Perdew, Burke, Ernzerhof.⁵⁵ For structural optimization we use 5-atom perovskite cells with $6 \times 6 \times 6$ k points in Monkhorst-Pack configuration⁷⁴ with an energy cutoff of 600 eV, and use the tetrahedron method with Blöchl corrections for Brillouin-zone integration.⁷⁵ For the original set of calculations we optimize only the volume, while enforcing $Pm\bar{3}m$ symmetry (i.e., a cubic lattice). We initialize the magnetic moment on the ions to a low spin state ($0.6 \mu_B$),

except for the transition metals, Sc–Zn, Y–Cd, and La–Hg, which are initialized to a high spin state ($5.0 \mu_B$). Since we mostly work with the smallest possible unit cell of 5 atoms, only ferromagnetic configurations can be represented. Most of the compositions we consider are nonmagnetic, and the up and down spin densities typically become equal after a few electronic iterations.

To obtain accurate Kohn-Sham gaps we calculate the density of states using a static calculation on the pre-optimized geometry with $12 \times 12 \times 12$ gamma point centered k points. The gaps were calculated by measuring the energy range for which there are zero states in both the spin-up and spin-down channel in the density of states above and below the Fermi level. Magnetization is calculated as the difference between the spin-up electron occupancy minus the spin-down occupancy in the usual collinear spin-polarized DFT setup. In addition to calculations for the ideal cubic perovskite structure, we also use fixed distorted cells with respectively tetragonal and a rhombohedral distortions, using, respectively, the ground state optimized structure of BaTiO₃ and PbTiO₃ scaled to the cubic equilibrium volume of the composition.

As described in the paper, 99 compositions are selected on basis of their Kohn-Sham gap being larger than 0.25 eV. For these compositions we perform a constant volume ionic and cell-shape relaxation for phases which were distorted tetragonally, rhombohedrally, or with the oxygen octahedra rotated along the (1,1,1) direction, giving the corresponding phase energies. For these calculations the cell-shape optimization is kept restricted to the cubic phase volume to avoid unphysically large c/a ratios due to shortcomings of the exchange-correlation functional.^{31,76}

Further screening criteria reduce the set of compounds to 49. This set is investigated for Born effective charge for the A - and B -site ions using both the Berry-phase algorithm^{77–81} and density functional perturbation theory (dfpt)^{82,83} as implemented in VASP. The results were compared and typically agree better than within 5%. The values obtained with dfpt are the ones used in plots.

For the spontaneous polarization P_s we follow the scheme by Resta *et al.*, and Vanderbilt and King-Smith.^{32,84} The quantity P_s is calculated in the tetragonal distortion as the change in macroscopic polarization as the ions move adiabatically from ideal nonpolar symmetric positions into their relaxed positions. During this adiabatic transformation the cell is fixed at the shape and volume previously found for the

tetragonally distorted cell. The macroscopic polarization for a given configuration is calculated using the implementation in VASP 5.2.11 with tag L_{CALCPOL}. However, a difficulty with these calculations is that the electronic contribution to the macroscopic polarization is only calculated modulus a fixed period.^{32,84} Our polarization direction z is the tetragonal distortion direction with lattice constant c . We use non-spin-polarized calculations (none of the systems considered are magnetic). In this case, the period along the z axis is $2c$ when using the polarization unit used in VASP ($e\text{\AA}$). Since it is possible that the change of the polarization across the adiabatic path is larger than this period, we calculate the macroscopic polarization at 10 configurations interpolated linearly across the shortest distance between the initial and final positions of the ionic positions in the transformation path. Let P_m^e be the electronic contribution to the macroscopic polarization along z . For each configuration along the path, we bring the calculated value of P_m^e into its minimum gauge by adding a term $2kc$, where k is the positive or negative integer that minimizes $|P_m^e|$. Following the transformation path, the number of times the minimum gauge values of P_m^e crosses the period boundary, n , is counted and taken to be positive if P_m^e crosses from positive to negative $+c \rightarrow -c$, and vice versa. The full electronic contribution to the spontaneous polarization is now given as $P_s^e = \Delta P_m^e + 2nc$, where ΔP_m^e is the difference in P_m^e between the start and end point configuration. For all the systems studied we only find $-1 \leq n \leq 1$, which means the use of 10 intermediate configurations is likely generally excessive for recovering the moduli terms. To get the full spontaneous polarization P_s a “pseudopotential ionic contribution” term is added, $\sum_{i=1}^N v_i \Delta z_i$, where N is the number of ions in the system, v_i is the valence of the pseudopotential used for ion i (given as ZVAL in the pseudopotential file), and Δz_i is the displacement of ion i in the z direction between the initial and the final position.

Furthermore, for the 49 selected compositions we calculate ionic displacement energy landscapes as discussed in Sec. II. This is done by displacing one or both of the A - and B -site ions in the ABO_3 perovskite structure along either the rhombohedral (1,1,1) or the tetragonal (0,0,1) displacement axis in the conventional cell. For these calculations the crystal structure is kept in its ideal cubic configuration, and only the ions are moved over a 5×5 grid, with no volume or ionic relaxation.

¹K. Uchino, *Ferroelectric Devices*, 2nd ed. (CRC Press, 2009).

²B. Jaffe, W. R. Cook, and H. Jaffe, *Piezoelectric Ceramics* (Academic Press, New York, 1971).

³K. Uchino, *Piezoelectric Actuators and Ultrasonic Motors* (Kluwer Academic, Boston, 1996).

⁴B. Noheda, D. E. Cox, G. Shirane, J. A. Gonzalo, L. E. Cross, and S.-E. Park, *Appl. Phys. Lett.* **74**, 2059 (1999).

⁵B. Jaffe, *J. Appl. Phys.* **25**, 809 (1954).

⁶G. Shirane, K. Suzuki, and A. Takeda, *J. Phys. Soc. Jpn.* **7**, 12 (1952).

⁷G. Shirane and K. Suzuki, *J. Phys. Soc. Jpn.* **7**, 333 (1952).

⁸G. E. Haertling, *J. Am. Ceram. Soc.* **82**, 797 (1999).

⁹T. Takenaka and H. Nagata, *Key Eng. Mater.* **157**, 57 (1999).

¹⁰R. E. Jaeger and L. Egerton, *J. Am. Ceram. Soc.* **45**, 209 (1962).

¹¹R. H. Dungan and R. D. Golding, *J. Am. Ceram. Soc.* **48**, 601 (1965).

¹²G. H. Haertling, *J. Am. Ceram. Soc.* **50**, 329 (1967).

¹³L. Egerton and C. A. Bieling, *Ceram. Bull.* **47**, 1151 (1968).

¹⁴B. Aurivillius, *Arkiv For Kemi.* **1**, 499 (1949).

¹⁵A. Wood, *Acta Crystallogr.* **4**, 353 (1951).

- ¹⁶C. F. Buhner, *J. Chem. Phys.* **36**, 798 (1962).
- ¹⁷T. Nitta, *J. Am. Ceram. Soc.* **51**, 626 (1968).
- ¹⁸B. A. Scot, E. A. Giess, G. Burns, and D. F. O’Kane, *Mater. Res. Bull.* **3**, 831 (1968).
- ¹⁹P. Hohenberg and W. Kohn, *Phys. Rev.* **136**, B864 (1964).
- ²⁰W. Kohn and L. J. Sham, *Phys. Rev.* **140**, A1133 (1965).
- ²¹G. Ceder, Y.-M. Chiang, D. R. Sadoway, M. K. Aydinol, Y.-I. Jang, and B. Huang, *Nature (London)* **392**, 694 (1998).
- ²²S. Curtarolo, D. Morgan, K. Persson, J. Rodgers, and G. Ceder, *Phys. Rev. Lett.* **91**, 135503 (2003).
- ²³D. Morgan, G. Ceder, and S. Curtarolo, *Meas. Sci. Technol.* **16**, 296 (2005).
- ²⁴A. Jain, S. Seyed-Reihani, C. C. Fischer, D. J. Couling, G. Ceder, and W. H. Green, *Chem. Eng. Sci.* **65**, 3025 (2010).
- ²⁵J. Greeley, T. F. Jaramillo, J. Bonde, I. Chorkendorff, and J. K. Nørskov, *Nature Mater.* **5**, 909 (2006).
- ²⁶G. K. H. Madsen, *J. Am. Chem. Soc.* **128**, 12140 (2006).
- ²⁷P. Groth, *Ann. Phys. Chem.* **217**, 31 (1870).
- ²⁸P. M. Goldschmidt, *Trans. Faraday Soc.* **25**, 253 (1929).
- ²⁹L. Bellaiche, A. García, and D. Vanderbilt, *Phys. Rev. Lett.* **84**, 5427 (2000).
- ³⁰S.-E. Park and T. R. ShROUT, *J. Appl. Phys.* **82**, 1804 (1997).
- ³¹H. Fu and R. E. Cohen, *Nature (London)* **403**, 281 (2000).
- ³²R. D. King-Smith and D. Vanderbilt, *Phys. Rev. B* **49**, 5828 (1994).
- ³³K. Momma and F. Izumi, *J. Appl. Crystallogr.* **41**, 653 (2008).
- ³⁴Y. Saito, H. Takao, T. Tani, T. Nonoyama, K. Takatori, T. Homma, T. Nagaya, and M. Nakamura, *Nature (London)* **432**, 84 (2004).
- ³⁵W. Liu and X. Ren, *Phys. Rev. Lett.* **103**, 257602 (2009).
- ³⁶K. Matsumoto, Y. Hiruma, H. Nagata, and T. Takenaka, *Jpn. J. Appl. Phys.* **45**, 4479 (2006).
- ³⁷L. Liu, H. Fan, L. Fang, X. Chen, H. Dammak, and M. P. Thi, *Mater. Chem. Phys.* **117**, 138 (2009).
- ³⁸R. E. Cohen, *Nature (London)* **358**, 136 (1992).
- ³⁹W. Zhong, D. Vanderbilt, and K. M. Rabe, *Phys. Rev. Lett.* **73**, 1861 (1994).
- ⁴⁰W. Zhong and D. Vanderbilt, *Phys. Rev. Lett.* **74**, 2587 (1995).
- ⁴¹A. García and D. Vanderbilt, *Phys. Rev. B* **54**, 3817 (1996).
- ⁴²U. V. Waghmare and K. M. Rabe, *Phys. Rev. B* **55**, 6161 (1997).
- ⁴³K. M. Rabe and E. Cockayne, *AIP Conf. Proc.* **436**, 61 (1998).
- ⁴⁴P. Ghosez, E. Cockayne, U. V. Waghmare, and K. M. Rabe, *Phys. Rev. B* **60**, 836 (1999).
- ⁴⁵M. Ghita, M. Fornari, D. J. Singh, and S. V. Halilov, *Phys. Rev. B* **72**, 054114 (2005).
- ⁴⁶G. Kresse and J. Furthmüller, *Vienna Ab Initio Simulation Package, Users Guide* (The University of Vienna, Vienna, 2007).
- ⁴⁷G. Kresse and J. Hafner, *Phys. Rev. B* **47**, 558 (1993).
- ⁴⁸G. Kresse and J. Hafner, *Phys. Rev. B* **49**, 14251 (1994).
- ⁴⁹Y. Liu, C.-N. Xu, K. Nonaka, and H. Tateyama, *Ferroelectrics* **264**, 331 (2001).
- ⁵⁰B. Noheda, L. Wu, and Y. Zhu, *Phys. Rev. B* **66**, 060103 (2002).
- ⁵¹S. V. Halilov, M. Fornari, and D. J. Singh, *Appl. Phys. Lett.* **81**, 3443 (2002).
- ⁵²Y. Suárez-Sandoval and P. K. Davies, *Appl. Phys. Lett.* **82**, 3215 (2003).
- ⁵³M. Fornari and D. J. Singh, *Phys. Rev. B* **63**, 092101 (2001).
- ⁵⁴D. I. Bilc and D. J. Singh, *Phys. Rev. Lett.* **96**, 147602 (2006).
- ⁵⁵J. P. Perdew, K. Burke, and M. Ernzerhof, *Phys. Rev. Lett.* **77**, 3865 (1996).
- ⁵⁶R. Armiento and A. E. Mattsson, *Phys. Rev. B* **72**, 085108 (2005).
- ⁵⁷A. E. Mattsson, R. Armiento, J. Paier, G. Kresse, J. M. Wills, and T. R. Mattsson, *J. Chem. Phys.* **128**, 084714 (2008).
- ⁵⁸J. P. Perdew, A. Ruzsinszky, G. I. Csonka, O. A. Vydrov, G. E. Scuseria, L. A. Constantin, X. Zhou, and K. Burke, *Phys. Rev. Lett.* **100**, 136406 (2008).
- ⁵⁹D. I. Bilc, R. Orlando, R. Shaltaf, G.-M. Rignanese, J. Íñiguez, and P. Ghosez, *Phys. Rev. B* **77**, 165107 (2008).
- ⁶⁰D. G. Pettifor, *Solid State Commun.* **51**, 31 (1984).
- ⁶¹C. Li, K. C. K. Soh, and P. Wu, *J. Alloys Compd.* **372**, 40 (2004)..
- ⁶²V. M. Goldschmidt, *Skriber Norske Videnskaps-Akad. Oslo, I. Mat.-Nat. Kl.* **8** (1926).
- ⁶³R. D. Shannon, *Acta Crystallogr. Sect. A* **32**, 751 (1976).
- ⁶⁴D. J. Singh, *Phys. Rev. B* **52**, 12559 (1995).
- ⁶⁵H. Fujishita and S. Katano, *J. Phys. Soc. Jpn.* **66**, 3484 (1997).
- ⁶⁶I. B. Bersuker, *The Jahn-Teller Effect* (Cambridge University Press, Cambridge, 2006).
- ⁶⁷S. M. Nakhmanson and I. Naumov, *Phys. Rev. Lett.* **104**, 097601 (2010).
- ⁶⁸S. Suzuki, T. Takeda, A. Ando, and H. Takagi, *Appl. Phys. Lett.* **96**, 132903 (2010).
- ⁶⁹G. Shirane and R. Pepinsky, *Phys. Rev.* **91**, 812 (1953).
- ⁷⁰U. von Barth and L. Hedin, *J. Phys. C* **5**, 1629 (1972).
- ⁷¹M. M. Pant and A. K. Rajagopal, *Solid State Commun.* **10**, 1157 (1972).
- ⁷²P. E. Blöchl, *Phys. Rev. B* **50**, 17953 (1994).
- ⁷³G. Kresse and D. Joubert, *Phys. Rev. B* **59**, 1758 (1999).
- ⁷⁴H. J. Monkhorst and J. D. Pack, *Phys. Rev. B* **13**, 5188 (1976).
- ⁷⁵P. E. Blöchl, O. Jepsen, and O. K. Andersen, *Phys. Rev. B* **49**, 16223 (1994).
- ⁷⁶Z. Wu and R. E. Cohen, *Phys. Rev. B* **73**, 235116 (2006).
- ⁷⁷R. D. King-Smith and D. Vanderbilt, *Phys. Rev. B* **47**, 1651 (1993).
- ⁷⁸D. Vanderbilt and R. D. King-Smith, *Phys. Rev. B* **48**, 4442 (1993).
- ⁷⁹R. Resta, *Ferroelectrics* **136**, 51 (1992).
- ⁸⁰R. Resta, *Rev. Mod. Phys.* **66**, 899 (1994).
- ⁸¹R. Resta, in “Berry Phase in Electronic Wavefunctions,” *Troisième Cycle de la Physique en Suisse Romande, Anne Academique 1995* (1996).
- ⁸²M. Gajdos, K. Hummer, G. Kresse, J. Furthmüller, and F. Bechstedt, *Phys. Rev. B* **73**, 045112 (2006).
- ⁸³S. Baroni and R. Resta, *Phys. Rev. B* **33**, 7017 (1986).
- ⁸⁴R. Resta, M. Posternak, and A. Baldereschi, *Phys. Rev. Lett.* **70**, 1010 (1993).